DOI: 10.1002/adma.200701363

# Shear-Induced Organization in Flexible Polymer Opals**

By *Otto L. J. Pursiainen, Jeremy J. Baumberg,* Holger Winkler, Benjamin Viel, Peter Spahn,* and *Tilmann Ruhl*

Synthesis of 3D opaline photonic crystals has developed into a standard procedure during the last decade.[1–5] However, the conventional methods suffer from multiple drawbacks, with cracking and polycrystallinity[6–9] leading to degradation of the optical properties of these photonic crystals through, e.g., scattering. These special difficulties in 3D photonic crystal fabrication have hindered the utilization of the technology in commercial applications, and such photonic information technology[10] is still in its infancy. Clearly there is a need for industrial-scale, high-yield methods for producing functional photonic crystals. A novel cost-effective large-scale technique to produce flexible opals through shear-ordering during compression, utilizing a core/shell approach based on polymers, has recently been developed[11,12] and further demonstrated to have possible applications, e.g., sensor, security, and structural color applications.[13]

In this Communication we present a key analysis of the 3D rheologically derived properties of shear-ordered opaline thin-film photonic crystals using optical tracking of the strain-induced anisotropy. Probing UV-surface diffraction combined with band-gap measurements reveals a complete picture of the unit cell changes under strain. The results demonstrate that our polymer opals consist of a coherently ordered ''super-domain'' characterized by a radial director vector and show anisotropic photonic behavior depending on the relative vectorial orientation of strain and director.

Shear-ordering of colloidal suspensions has been studied extensively in recent years.[14–17] In these systems the crystal ordering is dependent on both the applied shear profile and the strength of shear, and with suitable conditions long-range ordering is achieved, possibly with some dislocations or stacking faults. Our approach relies on the compression-induced shear-flow ordering of core/shell polymer particles resulting in highly-ordered solid photonic crystals with spectacular structural color features (Fig. 1a). We start with precursor core/shell particles composed of a polystyrene–polymethylmethacrylate (PS–PMMA) core and polyethylacrylate (PEA) shell. The detailed precursor preparation is described elsewhere.[11] By uniaxially compressing the precursor powder between two heated plates (Fig. 1b), we create a viscous shear flow in the polymer melt forcing the spheres to assemble into an *fcc*-lattice. The resulting structure formed here is a circular thin (ca. 300 μm) film disk (diameter 15 cm) of low-refractive-index-contrast *fcc*-crystal, with the PS–PMMA cores forming the lattice and the PEA filling the interstitial sites. In this photonic crystal film the (111) planes are oriented parallel to the compression plates.[11–13] The (111)-plane resonance wavelength can be tuned by varying the precursor PS–PMMA particle size, and the sample can be doped with nanoparticles leading to interesting photonic behavior.[18] In this paper we show results obtained from opals using 235 nm (sample VIS) and 355 nm (sample NIR) diameter precursor particles. Prior to the compression, crosslinking chemicals (e.g., benzophenone) are mixed into the precursor powder by extrusion and after compression are activated by UV illumination, which affects the interstitial PEA-crosslinking by generated radicals.[19] The formation of an elastomeric structure is achieved by crosslinking the PEA polymer through exposure to UV light (60 mW $cm^{-2}$ from an Osram Vitalux UV lamp for 15 minutes).

It is not a priori clear how the material flow originates during compression-initiated shear. In both steady-state shear and oscillatory shear between a stationary and a moving plate, two different regimes have been distinguished.[16] It has been suggested that in the low shear regime the lines of touching spheres ($\underline{\mathbf{n}}$) are perpendicular to the velocity flow ($\underline{\mathbf{v}}$) (Fig. 1d), whereas in the high-strain regime these lines of touching spheres are parallel to the velocity vector (Fig. 1e). The geometry is different in our uniaxial compression scheme but the strain profile is thought to be parabolic, yielding a Poiseuille-type flow with the minimum velocity at the plates, and the maximum velocity in the center of the melt[15] (indicated by arrows in Fig. 1b). During compression, crystallization starts from the compression plates (where the shear is at its highest) and proceeds further into the melt.[10] Extensive transmission electron microscopy (TEM) confirms that a quasi-ordered region forms around the mid-thickness of the melt owing to the decreasing shear, while closer to the opposite plate the shear increases again resulting in improved long-range order. The excellent volume *fcc* close packing shown

[*] Prof. J. J. Baumberg, O. L. J. Pursiainen
School of Physics and Astronomy
University of Southampton
Southampton, SO17 1BJ (UK)
E-mail: jjb12@cam.ac.uk

Dr. H. Winkler
Merck KGaA
Frankfurter Strasse 250, 64291 Darmstadt (Germany)

B. Viel, P. Spahn, Dr. T. Ruhl
Deutsches Kunststoff-Institut (DKI)
Schlossgartenstrasse 6, 64289 Darmstadt (Germany)

[**] This work was supported by EPSRC grant EP/C511786/1. O.L.J.P. acknowledges the support of Merck KGaA and Helsingin Sanomat Centennial Foundation.

ADVANCED MATERIALS

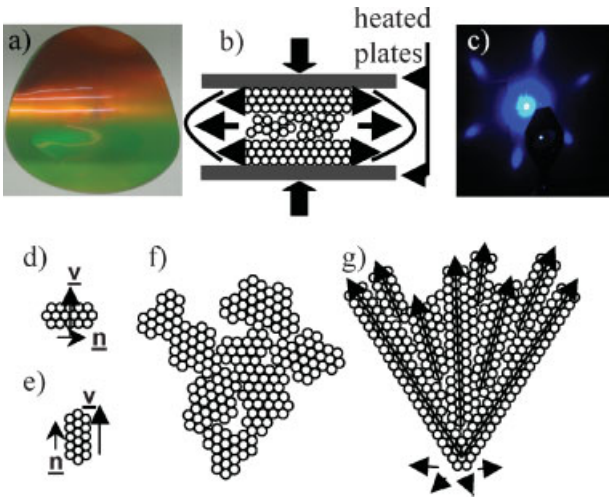


**Figure 1.** a) Bent 15 cm wide polymer opal film, revealing strong structural color features. b) Compression manufacturing of the polymer opal. The precursor powder is compressed between two heated (±150 °C) plates, leading to a parabolic shear profile indicated by the arrows. Ordering starts at the plates. c) Hexagonal diffraction pattern measured in reflection with a 248 nm laser. d) Low-shear, and e) high-shear regime. f) Multidomain ordering vs. g) radially oriented large-scale hexagonal ordering of the polymer opal into a superdomain during compression.

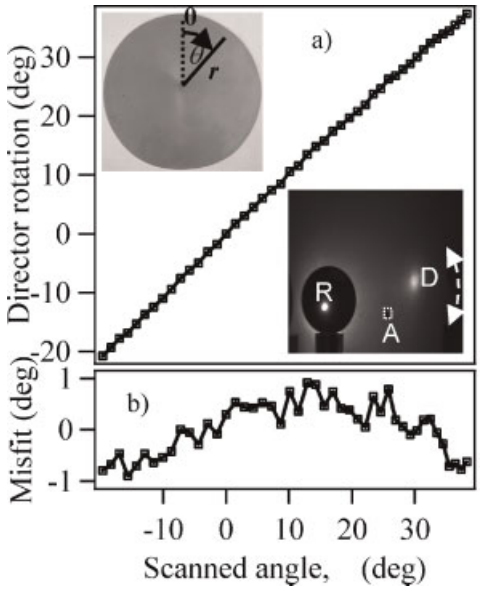


**Figure 2.** a) Extracted orientation of lattice director as a function of the angular position $\theta$ of the laser spot on the sample (left inset shows scan of laser spot). Right inset: Typical diffraction pattern with the reflected spot (R) viewed through a neutral density filter, input aperture (A), and the 1st order diffracted spot (D). b) Misfit between the lattice director orientation and the angular position $\theta$.

previously combined with low index contrast produces a new sort of photonic crystal with unusual properties.[18] The local ordering of the surface is verified to be hexagonal from the 6-fold diffraction pattern produced by an incident UV laser at 248 nm incident on the NIR sample (Fig. 1c). The penetration depth of the 248 nm UV photons is less than 1.5 μm,[20] and thus the resulting scattering originates only from surface order of the sample. Two different scenarios of how local hexagonal geometry is produced by shear-flow ordering can be pictured. Firstly, ordered regions can independently nucleate depending on the shear, with formation of polycrystalline domains across the film (Fig. 1f), which is characteristic of opal systems prepared by sedimentation or drying of colloidal suspensions.[6–9] In the other scenario the radially symmetric material flow during compression forces domain alignment, resulting in a ''super domain'' as large as the entire 15 cm sample with a macroscopic radial director profile ($\underline{\mathbf{n}}$ outwards, Fig. 1g). While it is clear that slip line dislocations or point vacancies are needed in this structure to accommodate the local hexagonal packing, the super-domain is characterized by a spatially coherent director vector, $\underline{\mathbf{n}}(r,\theta) = n\,\hat{r}$.

We study in detail the shear-induced ordering in our structures by spatially scanned surface-induced diffraction. For a frequency-doubled Ar-ion 248 nm laser, the UV photons can only Bragg diffract from the VIS sample for angles of incidence higher than 10°, so oblique illumination at 23° is used. The incoming laser spot (500 μm diameter) was scanned across the sample at fixed radii from the center of compression flow which is clearly seen in the disks (left inset, Fig. 2a). The resulting diffraction pattern for each incident location is recorded using a digital camera (right inset, Fig. 2a) from which the lattice director can be extracted using the measurement geometry. While we find the lattice pitch to be independent of position on the sample, the orientation of the director precisely tracks the radial velocity flow in the melt (Fig. 2a). In all cases we find the high-shear regime operates, in which the director is parallel to the velocity flow (Fig. 1g). Hence these polymeric photonic crystals form super domains on macroscopic length scales of many centimeters, in complete contrast to all other types of opals.[6–9]

This radial orientation of the director is found to be insensitive to its radial distance in the outflow (once out of the central region). However deviations in alignment of $\underline{\mathbf{n}}$ and $\underline{\mathbf{v}}$ (Fig. 2b) are seen on the scale of ±1° across a sector, and ±0.2° between points. In addition, we only ever observe a single diffraction spot (showing the lack of polycrystallinity) with an angular width matching that expected from $\underline{\mathbf{n}}(\theta)$ and the illuminated spot size. We thus conclude that dislocations are uniformly distributed on a small scale <10 μm, with large-scale nonuniformities in flow also imprinted onto the resulting director.

The elastomeric nature of these polymer opals allows study of how 3D ordered nanocomposites comprising solid spheres and stretchable filler influence the anisotropic elasto-optic properties. Changes from straining the polymer opal lattice in the film plane (imposing $s_x$) were tracked from the changes in the 6-fold surface diffraction of UV light. At the same time, induced vertical strains ($s_z$) were measured from the spectral shift of the reflection Bragg resonance from the (111)-planes (parallel to the surface) at visible wavelengths. Measuring both lateral and vertical strains allows us to track the volume

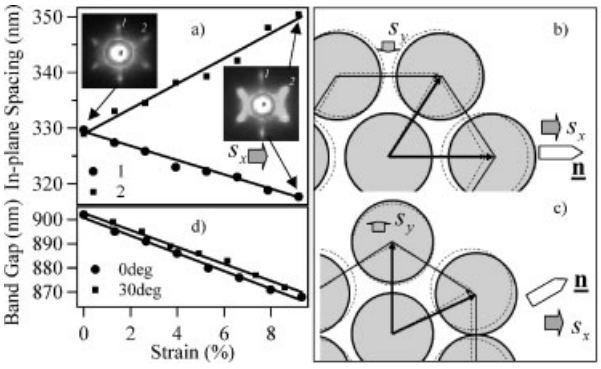


**Figure 3.** a) Changes in the in-plane spacing of the diffracting sphere rows on the opal surface as function of strain. Insets: corresponding diffraction patterns when probing the surface with 248 nm laser. b,c) Geometric changes in the unit cell of the PS spheres with 0% (black dashed lines) and 10% in-plane strain along *x* (blue solid lines) when $\underline{\mathbf{n}}$ is at 0° (b) or 30° (c) to $s_x$. d) Change in (111) lattice spacing with strain in the same conditions.

change optically. Furthermore, we can measure the deformation of the unit cell as the strain is applied at different in-plane orientations to the director (where $\phi_{sn}$ is the angle between strain $s_x$ and director $\underline{\mathbf{n}}$). In order to track the full effect on the different lattice planes in the unit cell, all 6-fold diffracted spots are recorded, necessitating the use of the larger-pitch NIR sample. A rectangular ($2.5 \times 1$ cm$^2$) section of sample was strained using a micrometer while clamped at both ends. From the diffraction patterns (Fig. 3a), the spatial distribution of high-strain regions within the unit cell, and how they depend on the orientation of the imposed stress, can be identified.

The characteristic diffraction patterns for a geometry where the applied strain $s_x$ is parallel to the director $\underline{\mathbf{n}}$ are shown in Figure 3a for strains of 0% (left inset) and 10% (right inset). The hexagonal surface structure diffracts the incident 248 nm photons into a hexagonal 6-fold symmetric pattern which is rotated by 30° with respect to the diffracting sphere surface geometry. Applying in-plane strain across the sample clearly breaks the symmetry of the diffraction pattern. Extracting the diffracted angles from these images using the measurement geometry, allows direct estimation of the sphere plane spacings, $a_{1,2}$. To illustrate the results, we consider here only the situations $\phi_{sn} = 0°$, 30° in which case two of these plane spacings are equal (the generic situation will be reported elsewhere, including analysis of the changes in the intensity of the diffracted spots which are expected from the sphere structure factors). For uniaxial strains $s_x$ parallel to the lattice director $\underline{\mathbf{n}}$, the change in the plane spacings corresponding to the two diffraction spots (labelled as *1* and *2*) are shown in Figure 3a. Initially the planes (which are at 60° to each other) are both 330 nm apart, but the strain modifies them differently with the 10% imposed strain in the *x*-direction leading to a +6.9% increase in the separation of spheres in plane *2*, while a −4.0% decrease in the separation of spheres in plane *1*. On the other hand, when applying the strain at 30° to the director, both plane spacings *1* and *2* increase by +2.8%, showing how structural anisotropy can be used to impose specific optical anisotropy. In all cases we find that the actual radial velocity flow direction gives identical results to those in the nominally symmetric directions at 60° to it, implying that surface packing is indeed hexagonal and initially unstrained.

Measuring also the angles between the diffracted samples and using well-known reciprocal lattice analysis[21] of the 3D sphere array allows extraction of the real space lattice vectors. Together with TEM analysis of the sphere diameters, this allows the unit cell to be completely reconstructed. We compare the two geometries of $\underline{\mathbf{n}}$ vs. $s_x$ (for $s_x = +10\%$) in Figure 3b and c, showing the movement of the individual spheres relative to each other. The behavior when $\phi_{sn} = 0°$ is intuitively clear: as the structure is elongated the horizontally stacked planes move closer to each other ($s_y < 0$, Fig. 3b). In contrast for $\phi_{sn} = 30°$, the lattice expands in every direction when strained along *x*. In the collinear case the surface unit cell area increases by +7.1% whereas for the case where the strain is 30° to the director, the area increases by +11.0%. We note that this strain is not uniformly distributed within the unit cell since the crosslinked PS spheres do not deform. We estimate that the increase in the PEA area is 29% (45%) for the 0° (30°) angle between the strain $s_x$ and director $\underline{\mathbf{n}}$ and thus the elastic limit is also anisotropic. It is also clear that the Poisson ratio $s_y/s_x$ changes sign between these two situations. While a full analysis of the $\phi_{sn}$ dependence is beyond the scope of the present paper, the principal orientations here already reveal the clear influence of elastically heterogeneous, photonically active composites. The imposition of the director alignment during radial material flow from uniaxial compression thus generates specific anisotropic elasto-optic properties.

Finally, to investigate the 3D nature of the strain-induced change in the polymer opal *fcc*-lattice we also measured the lattice spacing change in the direction perpendicular to the surface ($s_z$). The photonic stop-band or Bragg diffraction corresponding to the (111)-lattice planes produces a reflection peak whose spectral position in the NIR compares to the vertical plane spacing.[12] The results for the $s_x$ versus $\underline{\mathbf{n}}$ angles of 0° and 30° (Fig. 3d) show only 5% difference in the strain-induced changes in the (111)-plane spacing between the two experimental geometries. Combining this information with the unit cell areas calculated earlier reveal that the for +10% strain, the unit cell volume increases by +2.7% for $\phi_{sn} = 0°$, while by +6.7% for $\phi_{sn} = 30°$ (over twice as much). We conclude that the anisotropy of the unit cell expansion is mostly due to the 2D surface morphology, which depends strongly on the angle between the director and the strain vectors.

In conclusion, we investigate in detail the ordering process due to compression-flow-induced shear in manufacturing polymer opals. We clearly show that opals manufactured this way are characterized by a macroscopic director governing the global orientation of the hexagonal lattice. Such polymer photonic crystals have super domains with characteristic domain sizes over tens of square centimeters (and recently over meters. Furthermore, by examining strain-induced changes in the 3D geometry we conclude that the director dictates the anisotropy in the hexagonal lattice planes parallel

  

ADVANCED MATERIALS

to the surface but has little effect in the third dimension of the crystal. Such director-defined anisotropy could be utilized in a number of applications including strain sensing, security tagging, and photonic crystal enhanced birefringence.

## Experimental

*Director Measurement*: A frequency doubled Ar-ion laser (Coherent FRED) was operated at 248 nm. The beam was directed through the aperture (A) to be incident at 23° on the sample located at a distance of 52 mm from the screen. The resulting front-side diffraction pattern was recorded using a CCD camera (square pixels of $6.45 \times 6.45\ \mu m^2$) and a camera lens viewing the screen at an angle of 67°. The bright reflection spot (R) was attenuated using a ND2 filter.
*Strained Surface Diffraction*: The output of the doubled Ar-ion laser (see above) was directed perpendicularly onto the sample and the front diffraction pattern was recorded using Sony CyberShot Digital Still Camera DSC-S75. The sample was strained horizontally using a micrometer attached to a clamp setup.

Received: June 6, 2007
Revised: October 2, 2007
Published online:

[1] H. Miguez, F. Meseguer, C. Lopez, A. Mifsud, J. S. Moya, L. Vazquez, *Langmuir* **1997**, *13*, 6009.
[2] B. T. Holland, C. F. Blanford, A. Stein, *Science* **1998**, *281*, 538.
[3] J. E. G. J. Wijnhoven, W. L. Vos, *Science* **1998**, *281*, 802.
[4] G. Subramania, K. Constant, R. Biswas, M. M. Sigalas, K.-M. Ho, *Appl. Phys. Lett.* **1999**, *74*, 3933.
[5] P. Ni, P. Dong, B. Cheng, X. Li, D. Zhang, *Adv. Mater.* **2001**, *13*, 437.
[6] M. Müller, R. Zentel, T. Maka, S. G. Romanov, C. M. Sotomayor Torres, *Adv. Mater.* **2000**, *12*, 1499.
[7] V. N. Astratov, A. M. Adawi, S. Fricker, M. S. Skolnick, D. M. Whittaker, P. N. Pusey, *Phys. Rev. B* **2002**, *66*, 165215.
[8] Y. A. Vlasov, V. N. Astratov, A. V. Baryshev, A. A. Kaplyanskii, O. Z. Karimov, M. F. Limonov, *Phys. Rev. E* **2000**, *61*, 5784.
[9] M. A. McLachlan, N. P. Johnson, R. M. De La Rueb, D. W. McComb, *J. Mater. Chem.* **2004**, *14*, 144.
[10] J. D. Joannopoulos, P. R. Villeneuve, S. Fan, *Nature* **1997**, *386*, 143.
[11] T. Ruhl, P. Spahn, G. P. Hellmann, *Polymer* **2003**, *44*, 7625.
[12] T. Ruhl, P. Spahn, H. Winkler, G. P. Hellmann, *Macromol. Chem. Phys.* **2004**, *205*, 1385.
[13] O. L. J. Pursiainen, J. J. Baumberg, K. Ryan, J. Bauer, H. Winkler, B. Viel, T. Ruhl, *Appl. Phys. Lett.* **2005**, *87*, 101902.
[14] B. J. Ackerson, P. N. Pusey, *Phys. Rev. Lett.* **1988**, *61*, 1033.
[15] J. Liu, D. A. Weitz, B. J. Ackerson, *Phys. Rev. B* **1993**, *48*, 1106.
[16] M. D. Haw, W. C. K. Poon, P. N. Pusey, *Phys. Rev. E* **1998**, *57*, 6859.
[17] R. M. Amos, J. G. Rarity, P. R. Tapster, T. J. Shepherd, *Phys. Rev. E* **2000**, *61*, 2929.
[18] O. L. J. Pursiainen, J. J. Baumberg, J. Bauer, H. Winkler, B. Viel, P. Spahn, T. Ruhl, *Opt. Express* **2007**, *15*, 9553.
[19] K. Allmer, A. Hult, B. Ranby, *J. Polym. Sci. Part A* **1989**, *27*, 1641.
[20] S. Lazare, V. Granier, *J. Appl. Phys.* **1988**, *63*, 2110.
[21] C. Kittel, Introduction to Solid State Physics, 7th ed., Wiley, New York **1996**, Ch. 2.